# **Fracture Toughness of Thermoelectric Materials**

Guodong Li <sup>1,2</sup>, Qi An <sup>3</sup>, Bo Duan<sup>2</sup>, Leah Borgsmiller <sup>4</sup>, Muath Al Malki <sup>4,5</sup>, Matthias Agne <sup>4</sup>, Umut Aydemir <sup>6,7</sup>, Pengcheng Zhai <sup>1,2</sup>, Qingjie Zhang <sup>\*,1</sup>, Sergey I. Morozov <sup>8,9</sup>, William, A. Goddard III <sup>\*,9</sup>, and G. Jeffrey Snyder <sup>\*,4</sup>

<sup>1</sup>State Key Laboratory of Advanced Technology for Materials Synthesis and Processing, Wuhan University of Technology, Wuhan 430070, China.

<sup>2</sup>Hubei Key Laboratory of Theory and Application of Advanced Materials Mechanics, School of Science, Wuhan University of Technology, Wuhan, 430070, China.

<sup>3</sup>Department of Chemical and Materials Engineering, University of Nevada, Reno, Reno, Nevada, 89557, USA.

<sup>4</sup>Department of Materials Science and Engineering, Northwestern University, Evanston, Illinois 60208, USA.

<sup>5</sup>Mechanical Engineering Department, King Fahd University of Petroleum and Minerals, Dhahran, 31261, Saudi Arabia

<sup>6</sup>Department of Chemistry, Koç University, Sariyer, Istanbul, 34450, Turkey <sup>7</sup>Boron and Advanced Materials Application and Research Center, Koç University, Sariyer, Istanbul, 34450, Turkey

<sup>8</sup>Department of Physics of Nanoscale Systems, South Ural State University, Chelyabinsk, 454080, Russia

<sup>9</sup>Materials and Process Simulation Center, California Institute of Technology, Pasadena, California 91125, USA.

\*Corresponding authors: zhangqj@whut.edu.cn; wagoddard3@gmail.com; jeff.snyder@northwestern.edu ORCID: wag:0000-0003-0097-5716;

**Abstract:** The engineering applications of thermoelectric (TE) devices require TE materials possessing high TE performance *and* robust mechanical properties. Research on thermal and electrical transport properties of TE materials has made significant progress during the last two decades, developing TE materials on the threshold of commercial applications. However, research on mechanical strength and toughness has lagged behind, restricting application of TE materials.' Mechanical failure in these materials involves multi-scale processes spanning from atomistic scale to macro scale. We have proposed an integral stress-displacement method to estimate fracture toughness from intrinsic mechanical behavior. In this review, we summarize our recent progress on fracture toughness of TE materials. This is in three parts:

- (1) Predicting fracture toughness of TE materials from intrinsic mechanical behavior;
- (2) Intrinsic mechanical behavior and underlying failure mechanism of TE materials; and
- (3) Nanotwin and nanocomposite strategies for enhancing the mechanical strength and fracture toughness of TE materials.

These findings provide essential comprehensive understanding of fracture behavior from micro to the macro scale, laying the foundation for developing reliable TE devices for engineering applications.

**Keywords:** Fracture toughness; Thermoelectric materials; Intrinsic mechanical behavior; Nanotwins; Nanocomposites

#### 1. Introduction

Since the beginning of the 21<sup>st</sup> century, excessive exploitation and consumption of fuel oils have increased the energy crisis exacerbating various such environmental issues as global climate change, earthquakes, and acid rain [1-3]. Finding alternative clean energy is a major strategic near term goal to alleviate the energy crisis. Thermoelectric (TEs) materials to enable direct conversion between heat and electricity are recognized as candidates to play a significant role in the global solution to sustainable energy [1-3]. TE devices have important applications in new energy technology fields with new concept such as exhaust waste heat recovery, solar PV-TE hybrid systems, TE power generation, and mini refrigeration [2, 4-6]. These applications require TE devices possessing high TE efficiency *and* excellent mechanical reliability.

The conventional measure of TE device efficiency is closely related to the figure of merit (zT) of TE materials. Over the past two decades, developments in physics theory [7-18], breakthroughs in modern preparation technique [19-30], and discoveries of novel TE materials have led to remarkably enhanced zT value [19, 25, 31-46]. Many kinds of high-performance TE materials have been developed progressively to accelerate their commercial application opportunities. For example, dense dislocation arrays formed in Bi<sub>2</sub>Te<sub>3</sub> based room temperature TE materials significantly reduce the lattice thermal conductivity, improving its zT to 1.86 at  $\sim$ 300 K [29]. Also, developments of Multi-atomic filling [18], electronegative guest filling [41], and thermoelectric-magnetic effects have increased the zT value of skutterudite CoSb<sub>3</sub> to 1.7 at 850 K [47]. In addition, half-Heusler compounds like Ti(Zr,Hf)NiSn are good candidates for high temperature TE materials (zT > 1.0) due to its high TE properties and robust mechanical properties. Thus the conversion efficiency of an assembled half-Heusler module can reach 6.2% [42]. Moreover, MgAgSb alloys, based on inexpensive, abundant elements, recently were found to have zT values of  $\sim 1.3$  at  $\sim 500$  K, with devices showing a high conversion efficiency of 8.5% [48]. Another cheap and nontoxic TE material, Mg<sub>2</sub>(SiSn) alloys, shows a zT value of 1.4 through band convergence and effective defect engineering strategies [49, 50]. Obviously, the TE performance, zT, of TE materials has reached the level required for application.

The stability and reliability of TE devices under working environments rely on such mechanical properties as creep behavior, mechanical strength, and toughness.

Creep is a time-dependent mechanical deformation that takes place when the materials is subjected to a constant stress, typically below the yield point, for a sufficiently long time at 0.5-0.7 of the melting temperature, T<sub>m</sub> [51, 52]. Although the applied stress on a TE module may not be sufficient by itself to induce creep deformation, residual stresses from manufacturing may add up to a level high enough to induce such deformation. For instance, Bi<sub>2</sub>Te<sub>3</sub> prepared by selective laser melting (SLM) developed randomly oriented cracks on the top surface of the sample, a result of excessive tensile stresses imposed by the deep layer during solidification processes [53]. In addition to manufacturing residual stress, thermal stress plays a major role during the working phase of TE devices. This stress originates from the thermal expansion mismatch between different parts of the module, which is usually intensified during the thermal cycling, leading to cracking and increased internal resistance. Hatzikraniotis *et al.* observed a 14% drop in the output power of Bi<sub>2</sub>Te<sub>3</sub>, when cycling the hot side between 30°C and 200°C, while maintaining the cold side at room temperature [54]. Cracking and interdiffusion at the solder- metal interface gave rise to a 16% increase in the module's internal resistance, which eventually resulted in the drop of *zT* from 0.74 to 0.63 [54]. In a nutshell, when considering various contributors to the stress build-up in a TE module, creep

deformation may be crucial to the operational stability of such devices. Creep deformation was studied for several TE materials, including PbTe [55], Bi<sub>2</sub>Te<sub>3</sub>[56], Mg<sub>2</sub>Si-based [57], TAGS-85 [58], ZrNiSn-based [59] and Yb<sub>0.3</sub>Co4Sb<sub>12</sub> [60]. When kept at 400°C, PbTe shows a transition from diffusional to dislocation-based creep at 7.3 MPa, which is attributed to the bimodal grain distribution present in as-sintered samples [55]. In a similar vein, the microstructural anisotropy of Bi<sub>2</sub>Te<sub>3</sub> is thought to cause a change in the stress exponent from 4.2 to 6.2, when two similar samples were kept at the same temperature (400°C) within a similar stress range [56]. More recently, Malki *et al.* reported the creep resistance of the half-Heusler alloy Hf<sub>0.3</sub>Zr<sub>0.7</sub>NiSn<sub>0.98</sub>Sb<sub>0.02</sub>, in which the alloy sustained creep stresses up to 360 MPa with no macroscopic failure, with reported creep rates on the order of 10<sup>-8</sup>-10<sup>-7</sup> s<sup>-1</sup> [59]. The fine grain microstructure (1-7 μm) is thought to compel this half-Heusler alloy to deform via coble diffusional creep, with a stress exponent close to unity. Lastly, the creep resistance of Skutterudite alloy Yb<sub>0.3</sub>Co<sub>4</sub>Sb<sub>12</sub> was shown to be intermediate between the low-mid (PbTe, Bi<sub>2</sub>Te<sub>3</sub>) and high (Mg<sub>2</sub>Si, ZrNiSn) temperature thermoelectrics, dominated by the viscous glide of dislocations at 500°C within the stress range of 22-90 MPa [60].

Mechanical strength and toughness, which are the mechanical properties related to failure and fracture, are crucial to determine the reliability of TE devices. Poor mechanical strength and toughness can cause degradation of material properties and failure of TE devices [61-63]. Thus, many studies have been carried out to develop robust TE materials with high strength and toughness. Tang et al. adopted 3D printing technology to prepare highly textured bulk Bi-Sb-Te TE materials with a compressive strength of 91 MPa, much higher than those of single crystal (37 MPa) and Spark Plasma Sintered (SPS) polycrystalline samples (80 MPa) [64]. Sui et al. found that nanostructured  $\alpha$ -MgAgSb is a mechanically strong TE compound with a compressive strength of 390 MPa and nanoindentation hardness of 3.3 GPa, much stronger than other TE materials such as PbTe, SnTe, and Bi-Sb-Te [65]. Our group investigated the low-cycle stresscontrolled fatigue breakage of CoSb<sub>3</sub> under a compression-compression cycling loading condition and found ???[66]. Furthermore, nanocomposite technology has been found to effectively improve the mechanical properties of TE materials. Thus, Cai et al. found that adding tiny (xx nm) Fe<sub>3</sub>Si nanocomposites into p-type La<sub>0.8</sub>Ti<sub>0.1</sub>Ga<sub>0.1</sub>Fe<sub>3</sub>CoSb<sub>12</sub> can improve the indentation fracture toughness by 30% [67]. Li et al. found that adding 1.0 vol% nano-SiC into Bi<sub>2</sub>Te<sub>3</sub> can increase the Vickers hardness from 0.62 to 0.79 GPa, where a 0.5 vol% SiC added sample possess the highest Young's modulus of 42.7 GPa [68]. Our group found that introducing 1.0 vol.% nano-TiN into CoSb<sub>2.875</sub>Te<sub>0.125</sub> can enhance the flexural strength and fracture toughness by 31% and 40%, respectively, compared with the TiN-free samples [69]. Recently, a room temperature ductile inorganic semiconductor, α-Ag<sub>2</sub>S, was found to exhibit a metal-like ductility with 50% elongation under compression, offering a new promise for application in flexible electronic devices [70].

Compared with the research on TE performance, research on mechanical strength and toughness of TE materials is lagging behind, limiting the engineering applications of TE materials and devices. Among reports discussing mechanical strength and toughness of TE materials, most report experimental measurements. The mechanical strength of TE materials is much weaker than that of ceramics and the toughness is much lower than that of metals, leading to poor mechanical machinability of TE materials. Meanwhile, the mechanical properties of TE materials exhibits a relatively large dispersion, making it difficult to validate investigations of fracture behavior and its underlying mechanism. Therefore, to improve the mechanical strength and toughness of TE materials, it is urgent to develop a fundamental understanding of their fracture .

Mechanical failure of materials involves multi-scale processes, from atomistic to meso and to macro scale. We have proposed an integral stress-displacement method that can estimate the fracture toughness from ideal strength stress-displacement curves. In this review, we will summarize our recent work on fracture toughness of TE materials in three parts:

- Fracture toughness of TE materials from intrinsic mechanical behavior. We successfully applied the ideal stress-strain relations from DFT calculations to predict fracture toughness, leading to good agreement with the experiment measurements. This verifies that the prediction of ideal stress-strain relations at the atomic scale can be used to estimate rationally the fracture toughness.
- Intrinsic mechanical behavior and underlying failure mechanism of TE materials. We applied density functional theory (DFT) to investigate the tensile and shear deformation properties of a series of important TE materials. To derive the intrinsic mechanical properties at the atomic scale, including ideal strength and structural deformation mechanisms, we deformed these materials along various lattice orientations until structural failure.
- Two strategies for enhancing the mechanical strength and fracture toughness: Nanotwinning and nanocomposites. We proposed an effective nanotwinning strategy that can remarkably enhance the mechanical strength of such TE materials as Bi<sub>2</sub>Te<sub>3</sub> and InSb [71, 72]. In addition, we found that adding a small amount of nano-TiN particles into the GBs of CoSb<sub>3</sub> can lead to a co-existence of intergranular and transgranular fracture, resulting in a sharp increase of the fracture toughness of CoSb<sub>3</sub> [69].

# 2. Predicting fracture toughness from intrinsic stress-strain relationships

Fracture toughness is an inherent material property that describes a material's resilience to crack growth and ultimate mechanical failure. Due to the operational stress present in many applications of semiconductor materials, including TE materials, fracture toughness is an important engineering design metric.

Fracturing of a material ultimately occurs as a result of the finite strength of atomic bonds. When a material begins to fail, defects (e.g. cracks) are responsible for amplification of local stress states leading to fracture. The Griffith-Irwin relation recognizes that there is a thermodynamic criterion for fracture and that the fracture toughness,  $K_{Ic}$ , is an inherent material property that describes fracture conditions for a given material, independent of loading conditions and crack lengths.

Considering the case of plane-strain (thick plate assumption) under tensile deformation corresponding to the fracture toughness  $K_{Ic}$ , the well-known Griffith-Irwin relation takes the formula [73]:

$$K_{lc}^{2} = \frac{G_{lc}E}{1 - v^{2}} = \frac{2G_{lc}\mu}{1 - v} = \sigma_{gf}^{2}\pi\alpha_{c}$$
 (1)

Where E is the Young's modulus,  $\mu$  is the shear modulus,  $\nu$  is Poisson's ratio,  $\sigma_{gf}$  is the Griffith fracture stress for a critical crack length,  $\alpha_c$ , and Irwin called  $G_c$  the energy release rate [73].

Similarly, for fracture occurring under shear loading conditions, the mode II fracture toughness is defined as follows [74, 75]:

$$K_{IIc}^2 = \frac{2G_{IIc}\mu}{1 - \nu} \tag{2}$$

Griffith hypothesized that [76]  $G\sim2\gamma_s$ , where  $\gamma_s$  is the surface energy and the factor of 2 arises because two surfaces formed as a result of fracture. While this relation tends to hold for brittle materials, the "surface energy" relevant to fracture is, in fact, the energy required to break atomic bonds and form a new surface (i.e. G/2). While having units of  $[J/m^2]$ , this is not necessarily the same surface energy as  $\gamma_s$ . In a more general way, G can be estimated from the integral of a first-principles stress-displacement curve when integrated to the point of fracture (Fig. 1). This is written explicitly as:

$$G \sim \int_0^{fracture} \sigma \, dl$$
 (3)

G has units of energy per unit area and describes the energy required to create new "surfaces" at the atomic level. The generality of Eq. 3 means that the fracture energy in any arbitrary crystallographic direction can be determined. It would also be possible to apply this methodology to investigate the influence of various defect structures. We propose, however, that utilizing the fracture energy G of the weakest crystallographic plane is a good starting point for estimating fracture toughness (Fig. 1) [cite fracture paper in review].

# **Integral Stress-Displacement Method**

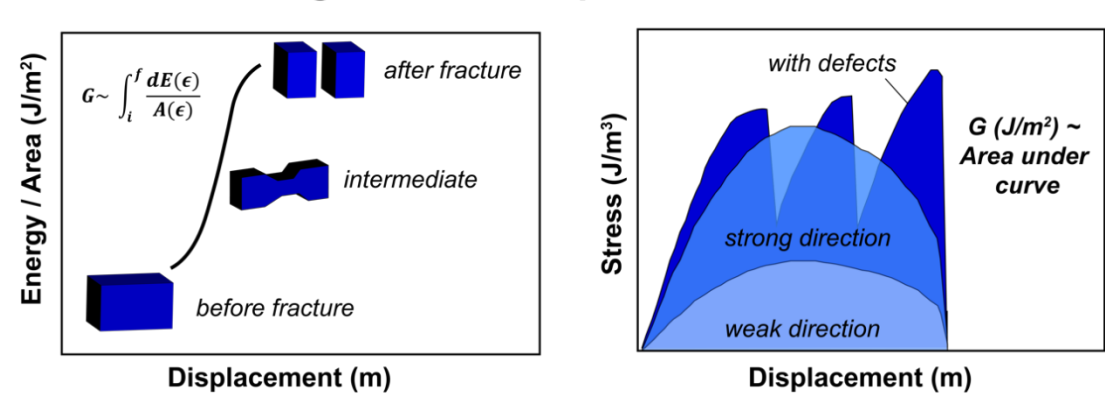


Figure 1 The integral stress-displacement method for estimating fracture toughness from ideal strength stress-displacement curves. In this case, the area under the ideal stress-displacement curve for a crystalline material is used as an approximation for *G*, capturing thermodynamically irreversible fracture processes in order to calculate fracture toughness. [Will need permission to reproduce figure]

This method for calculating fracture toughness was used for a variety of TE materials including PbTe, Bi<sub>2</sub>Te<sub>3</sub>, and CoSb<sub>3</sub> as well as for other materials such as TiC, TiN, and W**[cite fracture paper in review]**. The fracture toughness derived using this ideal stress-displacement were compared with polycrystalline and single crystalline experiments, and good agreement between this method and experiment was found, particularly for single crystal experiments (Fig. 2). Utilizing the fracture energy of the weakest crystallographic plane aptly provides a lower bound for the fracture toughness of a material and can be used to benchmark experimental results.

Thus, we successfully applied the ideal stress-strain relations from DFT calculations to predict such macro-mechanical properties as fracture toughness, that are in good agreement with experiment measurements. This verifies that prediction of the ideal stress-strain relations at the atomic scale can be used to rationally design the macroscopic mechanical properties.

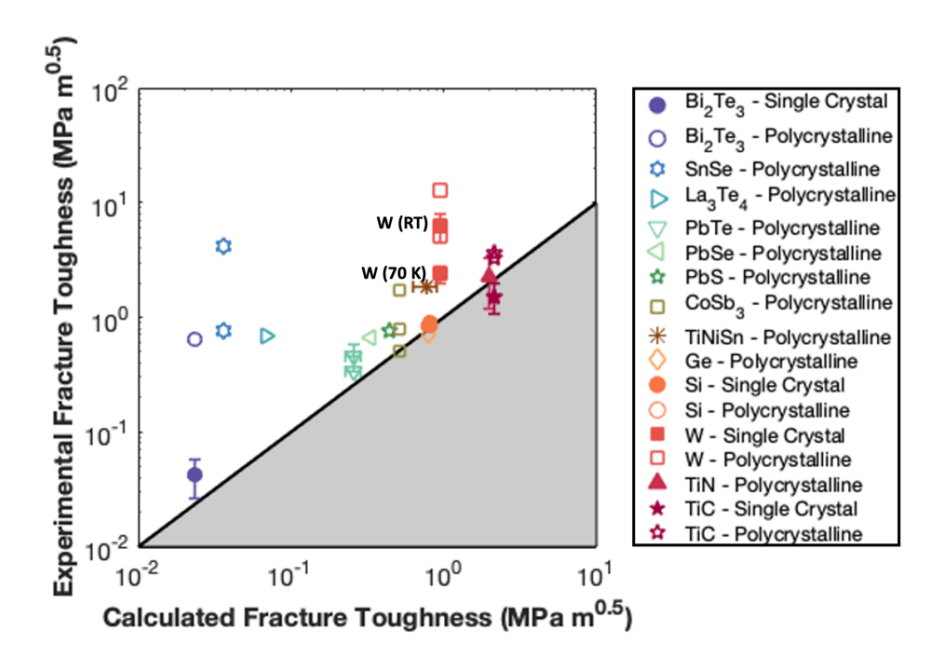


Figure 2 Comparison of fracture toughness values calculated using the ideal stress-displacement method with values from experiment. Filled in markers are indicative of single crystal experiments, which show good agreement with calculations. [

# 3. Intrinsic mechanical behavior and failure mechanism of TE materials at the atomic scale

Understanding the intrinsic structure-bonding relationships of a crystal is very important to elucidate the fracture mechanisms in these TE semiconductors as well as their fracture behavior.

We recently applied DFT to systematically investigate the intrinsic mechanical properties of 3-dimensional covalent compounds (TiNiSn[77], CoSb<sub>3</sub>[78], InSb[71]), 3-dimensional ionic compounds (PbS[79], Mg<sub>2</sub>Si, PbSe[79], PbTe[79],  $\alpha$ -MgAgSb[80], CuInTe<sub>2</sub>[81], La<sub>3</sub>Te<sub>4</sub>[82]), 2-dimensional ionic compounds (CaZn<sub>2</sub>Sb<sub>2</sub>[83], CaMg<sub>2</sub>Sb<sub>2</sub>[83], BiCuSeO[84], Mg<sub>3</sub>Sb<sub>2</sub>[83], In<sub>4</sub>Se<sub>3</sub>,  $\alpha$ -Ag<sub>2</sub>S[85]), and 2-dimensional van der Waals compounds (SnSe[86], Bi<sub>2</sub>Te<sub>3</sub>[72]). The intrinsic mechanical behavior is closely related to the nature of chemical bonding in these compounds [87]. We classified these compounds into four categories according to the structural and chemical bonding characteristics, leading to the ideal shear strengths summarized in Fig. 3. Generally, the ideal shear strength of TE materials follows the following trend: 3D covalent compounds > 3D ionic compounds > 2D ionic compounds > 2D van der Waals compounds. Moreover, the manner

in which these chemical bonds are softened and broken against external deformations can explain the mechanisms for deformation and failure of TE materials.

Next, we choose 2 typical TE compounds, brittle half-Heusler TiNiSn and ductile  $\alpha$ -Ag<sub>2</sub>S, to discuss their structural deformation and failure modes at the atomic scale.

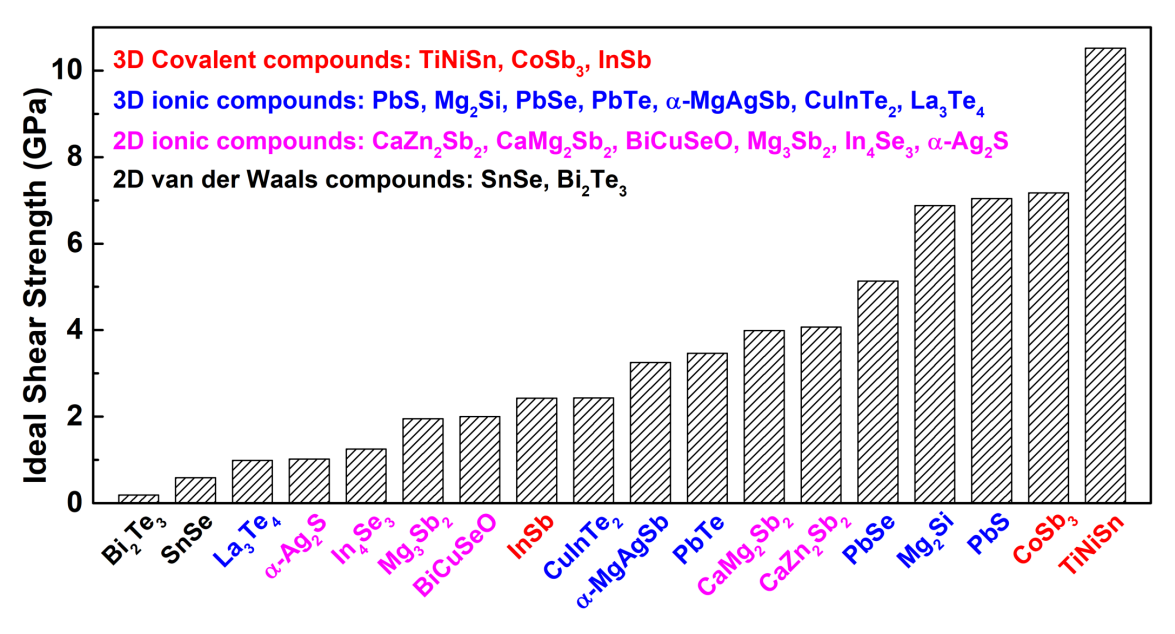


Figure 3 Summary of ideal shear strengths of important TE materials

### 3.1 Intrinsic mechanical properties of brittle half-Heusler TiNiSn

Ternary **half-Heusler** (HH) TiNiSn compounds crystalize in a cubic structure with the  $F\overline{43}m$  space group [88]. The chemical bonding can be described as a covalent zinc blende [NiSn]<sup>4-</sup> substructures, with Ti<sup>4+</sup> cations donating valence electrons to the sub-structures, as shown in Fig. 4(a). The shared electrons between Ni and Sn atoms suggest a strong covalent bonding interaction [77]. There are 8 TiSn cubic frameworks in TiNiSn. Half of them are filled with Ni atoms, while half are empty. If these 4 vacancies are totally filled by Ni atoms, the full Heusler TiNi<sub>2</sub>Sn structure is obtained.

We sheared TiNiSn along various slip systems such as (001)/<100>, (001)/<110>, and (111)/<1-10>, to investigate its deformation and failure mechanism, as shown in Fig. 4(b)-(e). At the small-strain stage (0 – 0.15 shear strain), the shear stress increases with shear strain, with nearly the same ratio, suggesting a similar elastic stiffness in three slip systems. Then, as the shear strain increases further, shear stress nonlinearly increases until the maximum stress point. Beyond that point, the shear stress gradually decreases, indicating structural yielding. We found that shearing along the (111)/<1-10> slip system leads to the lowest ideal shear strength of 10.52 GPa, much lower than those of the other two systems (Fig. 4(b)). At 0.232 shear strain corresponding to the ideal shear strength, the TiSn framework is distorted to resist the shear deformation (Fig. 4(c)). With further increasing shear strain, the TiSn framework is further distorted, while the stiffness gradually softens until reaching the shear strain of 0.323 (Fig. 4(d)). This corresponds to the structural yielding stage (0.232 – 0.323 strain). At the fracture strain of 0.334, the TiSn framework cannot resist the deformation, leading to failure. The empty TiSn framework collapses, releasing the shear stress and leading to shear failure of TiNiSn (Fig. 4(e)). Fig. 4(f) shows the typical bond lengths

against shear strain. Some bonds such as Ni2–Ti3, Ni2–Sn7, and Ni1–Ti9 bonds are stretched slightly, with the bond lengths increasing from 2.58 to 2.61 Å. This tiny bond change shows clearly that these bonds contribute little to the resistance of the deformation, explaining that shearing along the (111)/<1-10> slip system has the lowest ideal shear strength. The Ti9–Sn7 and Ti3–Sn3 bonds are stretched rapidly from 2.97 to 3.79 Å, with a large stretching ratio of 27.61% before failure, indicating a strongly softened bond. At the fracture strain of 0.334, these two bonds break, with deconstruction of the TiSn framework, resulting in failure of TiNiSn.

Replacing Ti with Hf and Zr atoms is confirmed to be an effective approach to improve the TE properties of TiNiSn [42]. Here, we investigated the role of these alloying elements on mechanical properties of the TiNiSn compound, as shown in Fig. 4(g). The (Ti, Hf, Zr) alloys show more robust mechanical properties, which we attribute to the enhanced rigidity of the TiSn framework after alloying with Hf and Zr. Specially, Hf atom seems more effective than Zr atom at strengthening TiNiSn, because Ti<sub>0.5</sub>Hf<sub>0.5</sub>NiSn shows a higher mechanical strength than Ti<sub>0.5</sub>Zr<sub>0.5</sub>NiSn. However, all the alloying systems exhibit a dramatically decreased shear stress after the structural yielding process, suggesting that Hf and Zr atoms do not significantly affect the failure mechanism of TiNiSn.

We further calculated the structural rigidity to quantitatively understand how alloying influences the mechanical strength of TiNiSn, as shown in Fig. 4(h). The structural rigidity (R) can be estimated by  $R = \sum_{i} k_i n_i$ , where i is the bond type in the structure,  $k_i$  is the stretching force

constant of the *i* bond, and  $n_i$  is the number of the *i* bond in the unit cell, easily obtained from the structure. We applied the ATAT code [89] to calculate the force constant in (Ti, Hf, Zr)NiSn systems. Fig. 4(h) clearly shows that the mechanical strength increases with increasing structural rigidity. Hf<sub>0.5</sub>Zr<sub>0.5</sub>NiSn has the highest structural rigidity of 152.4 eV/Å<sup>2</sup>. This explains why this structure has the highest ideal strength of 12.17 GPa (Fig. 4(g)). Alloying Ti by Hf and Zr can enhance the structural rigidity, strengthening TiNiSn. The structural rigidity of Ti<sub>0.5</sub>Hf<sub>0.5</sub>NiSn is higher than that of Ti<sub>0.5</sub>Zr<sub>0.5</sub>NiSn, confirming that Hf element is much more effective than Zr in strengthening TiNiSn.

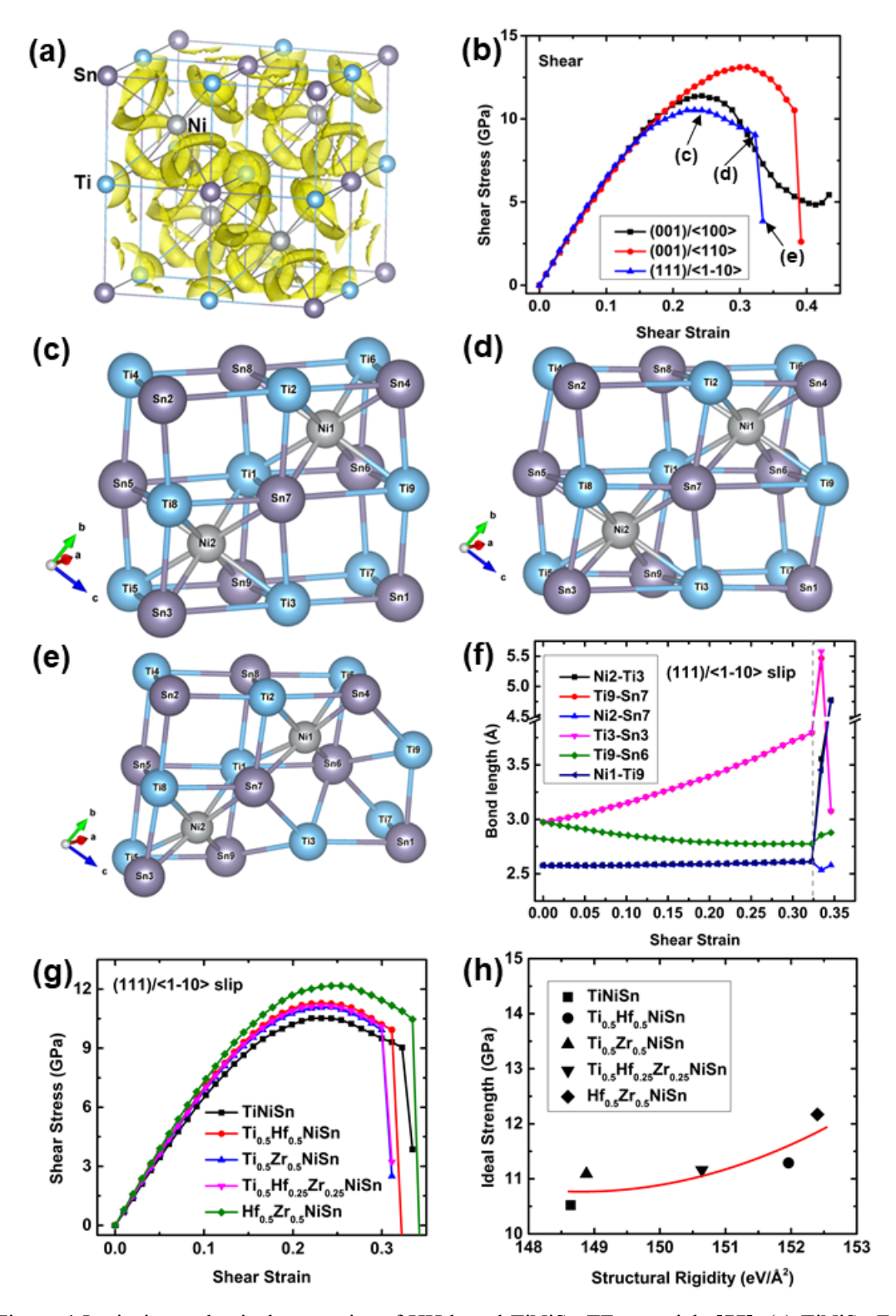


Figure 4 Intrinsic mechanical properties of HH based TiNiSn TE materials [77]. (a) TiNiSn Framework with calculated isosurfaces (at the value of 0.45) of the electron localization function (ELF). (b) Calculated shear stress – strain responses of TiNiSn along different slip systems. The atomic structures of TiNiSn along the (111)/<1-10> slip system at (c) shear strain of 0.232 corresponding to the ideal shear strength, (d) shear strain

of 0.323 before failure, and (e) failure strain of 0.334. (f) The average bond lengths in TiNiSn against shear strain. (g). The role of alloying Hf and Zr on mechanical properties of TiNiSn. (h). The ideal shear strength as a function of structural rigidity of (Ti, Hf, Zr)NiSn TE materials. The red line guides the eyes.

## 3.2 Intrinsic mechanical properties of ductile compound α-Ag<sub>2</sub>S

The ductile 2-dimensional ionic compound  $\alpha$ -Ag<sub>2</sub>S crystalizes in a monoclinic structure with  $P2_1/c$  (14) space group at room temperature. Fig. 5(a)-(b) show the structure along a-b and b-c plane, respectively. The computed electron localization function (ELF) shows that the isosurfaces are localized around the S atom, suggesting a typical ionic bonding interaction between Ag and S atoms. As shown in Fig. 5(a),  $\alpha$ -Ag<sub>2</sub>S is a layered structure with the "zigzag"-like Ag-S framework stacked along the a axis, which are linked with Ag-S bonds (2.67 Å). The inner-layered structure consists of distorted Ag-S octagons with the ionic Ag-S bond lengths of 2.41 and 2.52 Å, respectively (Fig. 5(b)).

The stress responses against shear strain and tensile strain are shown in Fig. 5(c) and (d), respectively. We find the (100)[010] and (001)[010] slip systems to have the same ideal strengths of 1.02 GPa and that they strongly resist deformation until the shear strain of 1.1 and 1.2, respectively. This suggests that  $\alpha$ -Ag<sub>2</sub>S processes strong ductile characteristic, agreeing well with experiment showing that  $\alpha$ -Ag<sub>2</sub>S is ductile at room temperature [70]. Under tension, the ductility along the [100] direction is much weaker than shearing along the (100)[010] and (001)[010] slip systems. This explains why  $\alpha$ -Ag<sub>2</sub>S shows a much smaller elongation of 4.2% under tension but over 50% strain under compression [70].

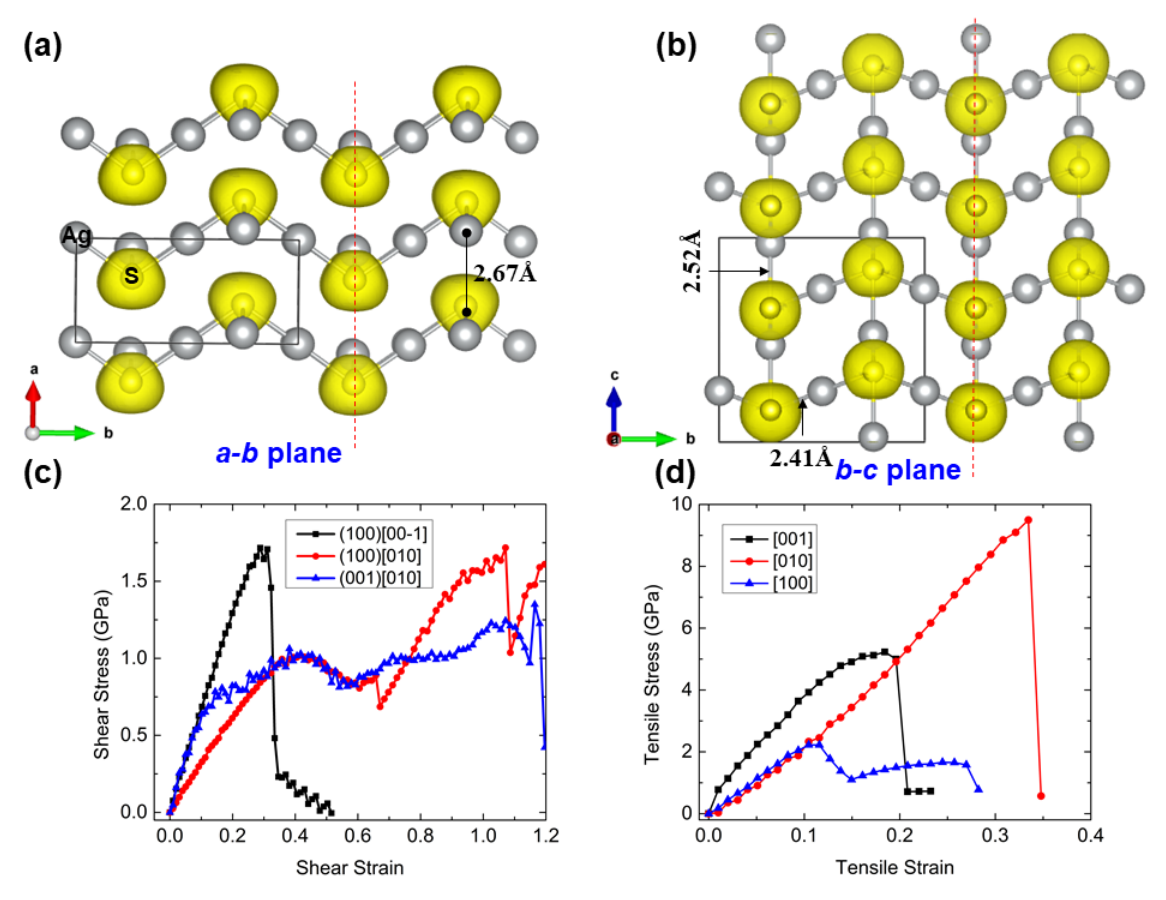


Figure 5 Crystal structure of  $\alpha$ -Ag<sub>2</sub>S with calculated isosurfaces (at the value of 0.65) of the ELF (a) along the *a-b* plane and (b) along the *b-c* plane. (c) Shear stress – strain relationships along different slip systems. (d) Tensile stress – strain relationships along different tensile systems. Reproduction permitted by NPG

We investigated the atomic configurations and bond-responding processes along two slip systems, (001)[010] and (100)[010], to explore the underlying ductile mechanism of  $\alpha$ -Ag<sub>2</sub>S, as shown in Fig. 6 and 7. Fig. 6 shows the pure shear deformation mechanism along the (001)[010] system, which is an inner-layered shearing system. The Ag-S octagons are distorted coordinating with shear strain without breaking Ag-S bonds (Fig. 6(b)), while the Ag1–S1–Ag3 angle is bent highly, enabling shear strain. As the shear strain increases to 0.417, the Ag1–S1–Ag3 angle is remarkably bent from 76.5° to 110.4°, while the Ag2–S1–Ag3 angle is slightly shrunk from 76.5° to 71.4° (Fig. 6(f)). Then, the Ag1–S1–Ag3 angle bends further to 148.6° before failure. However, the structure can retain its integrity because no bonds break. At the failure strain of 1.196, the Ag4–S1 length increases sharply to 4.35 Å (Fig. 6(e)), collapsing the Ag-S octagon framework and leading to failure of  $\alpha$ -Ag<sub>2</sub>S (Fig. 6(d)). The shear deformation in Fig. 6 shows clearly that the bending of the Ag1–S1–Ag3 angle dominates the plastic mechanism of  $\alpha$ -Ag<sub>2</sub>S for shearing along (001)[010].

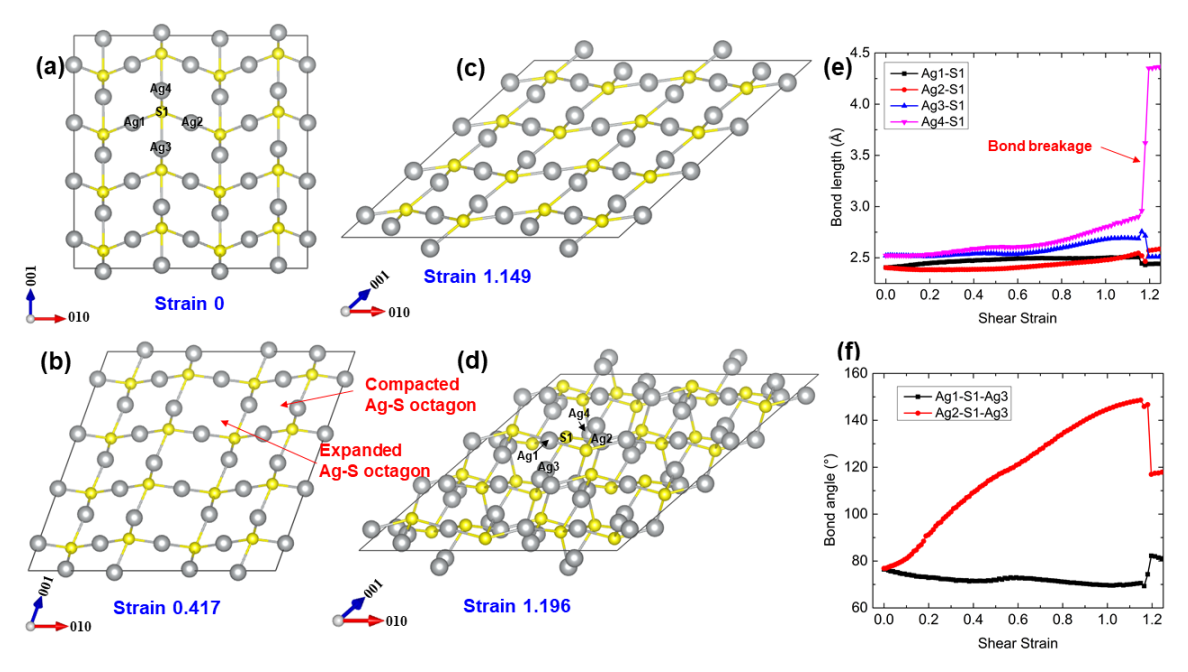


Figure 6 Deformation and failure of  $\alpha$ -Ag<sub>2</sub>S along the (001)[010] slip system [85]. (a) The intact structure at 0.0 shear strain. (b) Atomic structure at 0.417 shear strain, corresponding to the ideal strength. (c) Atomic structure at 1.149 shear strain, before the structural failure. (d) Atomic structure at the failure strain of 1.196. (e) The typical bond lengths (Ag1-S1, Ag2-S1, Ag3-S1, and Ag4-S1) as a function of shear strain. (f) The Ag1-S1-Ag3 and Ag2-S1-Ag3 bond angles as a function of shear strain. Reproduction permitted by NPG

Similarly, Fig. 7 displays the atomic configuration and bond-responding process along the (100)[010] slip system, which is an inter-layered shear system. With increasing shear strain, the stacked Ag-S frameworks slide past each other resisting shear deformation (Fig. 7(b)). It is noted that the Ag1 and Ag5 move rapidly towards each other during the shear process. At 0.671 shear strain, the Ag1–Ag5 length decreases to 3.15 Å. This length is only 8.9% larger than the Ag–Ag bond length (2.89 Å) in metallic Ag, suggesting that a new Ag1–Ag5 metallic bond forms at 0.671 shear strain. This newly formed bonding starts to improve the interaction between these stacked Ag-S frameworks. With the shear strain increasing to 1.087, the Ag1–Ag5 length reduces continuously to 2.87 Å, which is even shorter than the Ag–Ag length (2.89 Å) in metal Ag, completely coupling the stacked Ag-S frameworks. This strain-stiffening can effectively suppress the slippage between stacked Ag-S frameworks, maintaining the structural integrity (Fig. 7(c)). At the failure strain of 1.102, the Ag2–S1 bond breakage leads to the failure of α-Ag<sub>2</sub>S (Fig. 7(d)). The shear deformation in Fig. 7 clearly shows that the newly form Ag–Ag bonding is the origin of the ductile behavior of α-Ag<sub>2</sub>S for shearing along (100)[010].

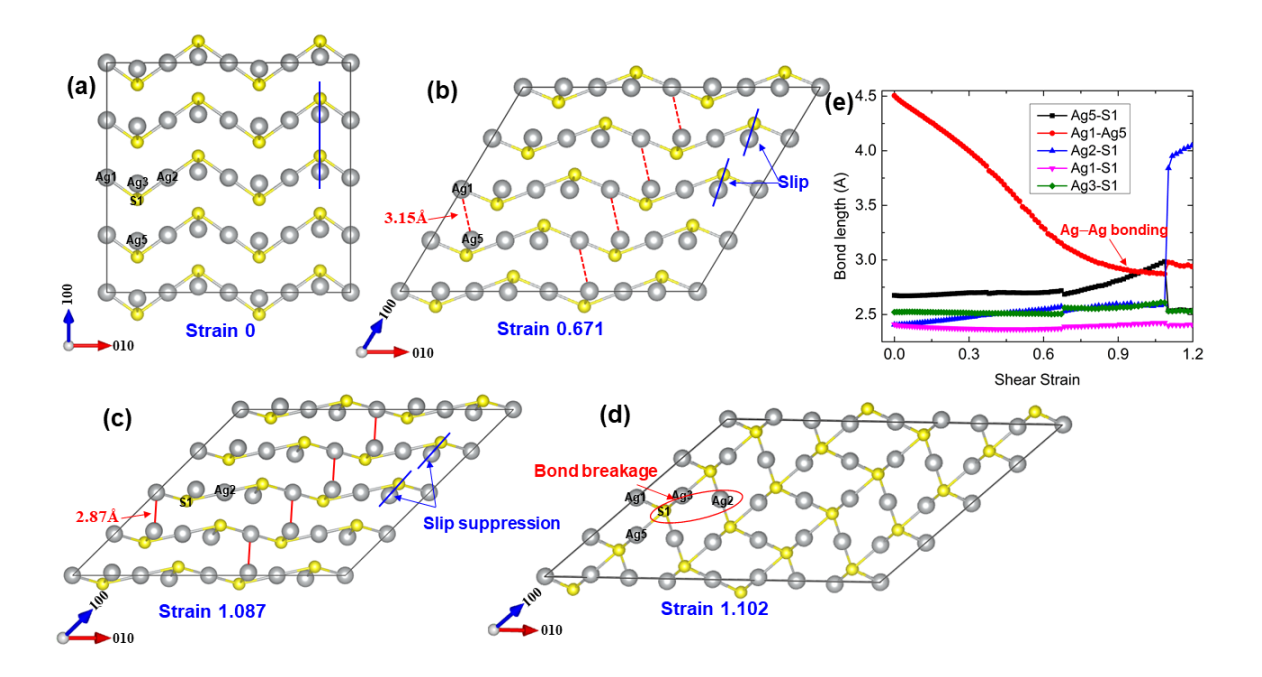


Figure 7 Deformation and failure of  $\alpha$ -Ag<sub>2</sub>S along the (100)[010] slip system [85]. (a) The intact structure at 0.0 shear strain. (b) Atomic structure at 0.671 shear strain, at which the newly formed Ag1-Ag5 bond starts to strengthen the structure. (c) Atomic structure at 1.087 shear strain, before the structural failure. (d) Atomic structure at the failure strain of 1.102. (e) The typical bond lengths (Ag5-S1, Ag1-Ag5, Ag2-S1, Ag1-S1, and Ag3-S1) as a function of shear strain. Reproduction permitted by NPG

In metals, the mechanism for plastic deformation is slip induced dislocations [90]. This requires materials with easy slip pathways and good structural integrity. We found  $\alpha$ -Ag<sub>2</sub>S to be ductile, which we attribute to the following two mechanisms.

- (i) Low ideal strength and multiple slip pathways. The ideal shear strength of  $\alpha$ -Ag<sub>2</sub>S is only 1.02 GPa, which is comparable with those of Cu, Al, and Mg metals [87, 91]. In addition, two most likely slip systems, (001)[010] and (100)[010], create easy pathways for slip.
- (ii) Retaining structural integrity during the whole shear process. During the inner-layered shearing, there is easy movement of Ag-S octagon framework without breaking Ag-S bonds, retaining structural integrity (Fig. 6). During inter-layered shearing, newly formed Ag-Ag bonds holds stacked Ag-S frameworks together, suppressing slippage between stacked Ag-S frameworks, while maintaining the structural integrity (Fig. 7).
- 4. Strategies for enhancing the mechanical strength and fracture toughness of TE materials

### 4.1 TBs strengthening TE materials

We found nanotwinned Bi<sub>2</sub>Te<sub>3</sub> based TE material to possess superior TE performance and robust mechanical properties [92]. This suggests that TBs might play a significant role in enhancing the mechanical properties of TE materials, motivating exploring the underlying mechanism.

We applied DFT to determine the mechanism underlying why TBs super strengthen Bi<sub>2</sub>Te<sub>3</sub>, as shown in Fig. 8. First, we established the nanotwinned structure of Bi<sub>2</sub>Te<sub>3</sub> with TBs along the [702] plane. based on the HRTEM figure (Fig. 8(a)-(b)). Along the TB plane, two covalent

Te1-Te1 bonds are formed with bond lengths of 3.48 Å, which further couples the five layered Te1-Bi-Te2-Bi-Te1 substructures (Fig. 8(a)). The shear stress - strain curves show that nanotwinned Bi<sub>2</sub>Te<sub>3</sub> is much stronger than the single crystalline Bi<sub>2</sub>Te<sub>3</sub>. The ideal strength of single crystalline Bi<sub>2</sub>Te<sub>3</sub> is 0.19 GPa, but it can be strengthened to 0.6 GPa from nanotwinning. In the elastic stage (from 0 to 0.04 shear strain), we found the elastic moduli for nanotwinned Bi<sub>2</sub>Te<sub>3</sub> is 59% higher than that of single crystalline Bi<sub>2</sub>Te<sub>3</sub>, further illustrating the TB strengthening effect. This TBs strengthening effect (Fig. 8(c)) agrees well with experimental observations showing that the flexural strength and compressive strength of (Bi,Sb)<sub>2</sub>Te<sub>3</sub> can be strengthened greatly through structural defects such as the nanotwinned structure (Fig. 8(d)). To illustrate this strengthening effect, we extracted the structural patterns at critical strains and typical bonding responses during the shear process (Fig. 8(f)-(i)). The lower half part of nanotwinned Bi<sub>2</sub>Te<sub>3</sub> shears along the same direction as bulk Bi<sub>2</sub>Te<sub>3</sub>, leading to stretching of the Te<sub>1</sub>(2)-Te<sub>1</sub>(3) and Te<sub>1</sub>(6)-Te<sub>1</sub>(7) bonds (Fig. 8(f)). The upper half part shears along the opposite direction, leading to a compression of the Te1(1)-Te1(2) and Te1(4)-Te1(5) bonds (Fig. 8(f)). The stretching ratio of the newly formed Te1(2)-Te1(3) bond is much smaller than the Te1(6)-Te1(7) van der Waals bond, indicating the strong interaction between substructures can be retained with increasing shear strain, giving rise to a much higher shear stress in nanotwinned Bi<sub>2</sub>Te<sub>3</sub> compared with that in bulk Bi<sub>2</sub>Te<sub>3</sub>. In addition, the strong Te1(1)–Te1(2) and Te1(2)–Te1(3) bonds can effectively suppress the softening of the van der Waals Te1-Te1 bonds near the TBs. These lead to a super-strengthened nanotwinned Bi<sub>2</sub>Te<sub>3</sub> (0.60 GPa), triple the ideal strength of its single crystal (0.19 GPa). We notice that this strain-stiffening effect is found in inorganic crystalline solids [93], where the enhanced material strength arises mainly from newly formed atomic bonds under large deformations. At 0.134 shear strain, the Te1(2)-Te1(3) bond stretching ratio increases sharply from 8% to 17%. This suggests a highly softening or non-bonding interaction (Fig. 8(h)), leading to a sudden drop of the shear stress (Fig. 8(e)). At 0.145 shear strain, the breaking of the Te1(1)–Te1(2) bond totally destabilizes the TBs and gives rise to structural failure (Fig. 8(i)).

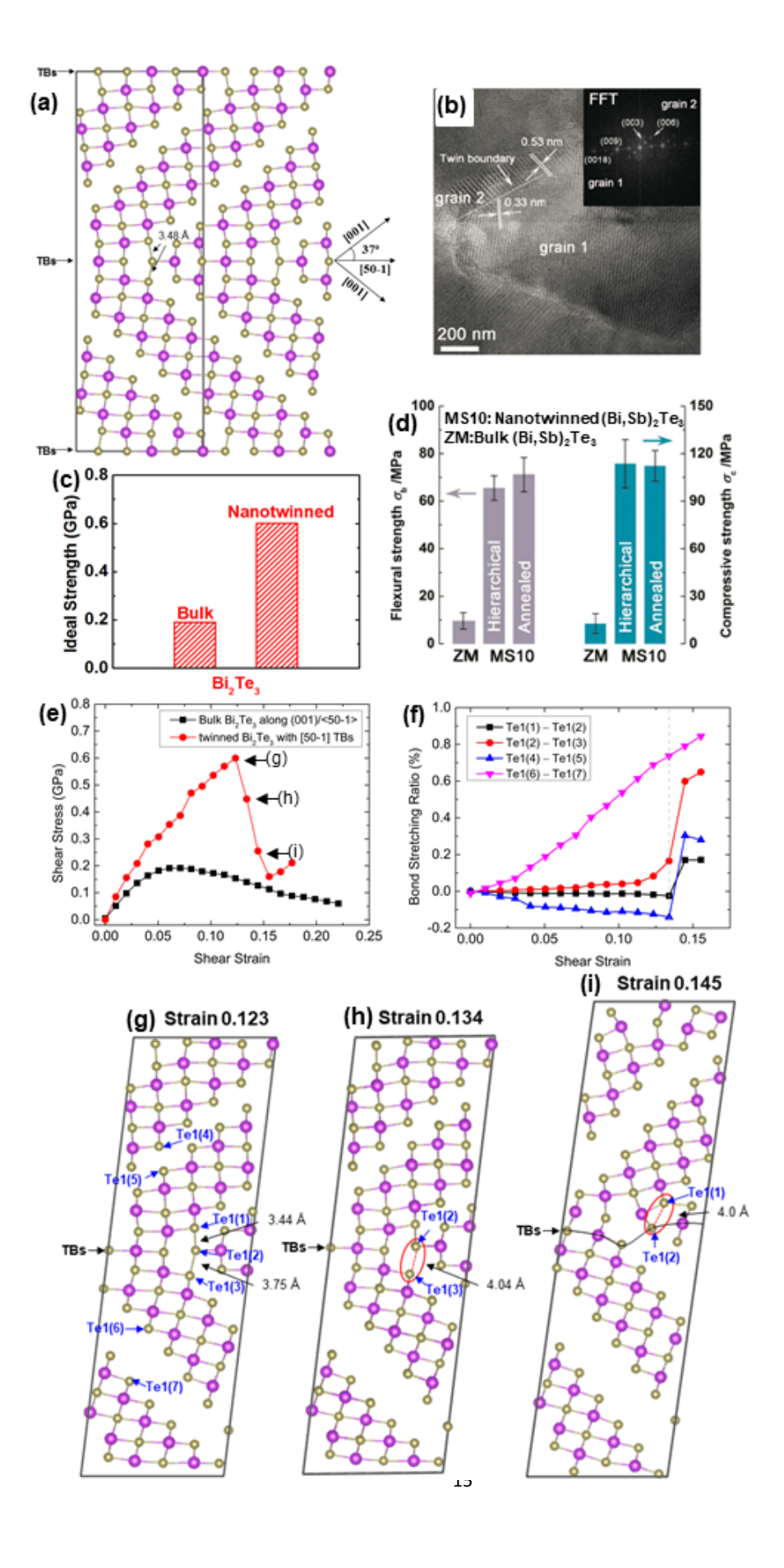


Figure 8 Nanotwin super strengthening of  $Bi_2Te_3$  [72]. (a) Structure of nanotwinned  $Bi_2Te_3$  established from DFT. (b) HRTEM image of twinned structure of  $Bi_2Te_3$  based TE material [92]. (c) Predicted high strength of nanotwinned  $Bi_2Te_3$  from DFT. (d) Experimental flexural and compressive strengths of the nanotwinned and bulk  $Bi_2Te_3$  [92]. (e) Shear-stress – strain relationships of nanotwinned  $Bi_2Te_3$  with a comparison to bulk  $Bi_2Te_3$ . (f) The critical bond changes with shear strain. Structural pattern at (g) 0.123, (h) 0.134, and (i) 0.145 shear strain, respectively. Reproduction permitted from APS and Willey.

# 4.2 Nanocomposite Strengthening of TE materials

Adding nano-scaled high-strength grains into the matrix was found to be an effectively approach to strengthen the matrix material [67, 69, 94]. In our experimental work, we added a small amount of nano TiN into CoSb<sub>2.875</sub>Te<sub>0.125</sub> TE material. We found that introducting 1.0 vol% TiN can increase the zT value by 10% compared with the value of TiN-free sample. We attribute this to the reduction of thermal conductivity resulting from the nano-particle selective phonon scattering mechanism [69]. More important, we found that the measured flexural strength and fracture toughness increase gradually with TiN content, as shown in Fig. 9. Specifically, with a 1.0 vol% nano-TiN ratio, the flexural strength increases from 116.8 MPa to 148.2 MPa, a 31% improvement compared with that of TiN-free sample. The fracture toughness increases from 1.06 MPam<sup>1/2</sup> to 1.47 MPam<sup>1/2</sup>, a 40% improvement compared with that of TiN-free sample. The fracture subfigure embedded in Fig. 9 shows clearly a pinning effect that results from the introduction of TiN nano-particles into CoSb<sub>2.875</sub>Te<sub>0.125</sub> TE material. This creates mechanically interlocked interfaces between TiN particles and matrix, increasing the resistance against crack growth. This can significantly change the crack propagation path, leading to a transgranular fracture (Fig. 9), thereby resulting in a sharp increase of the fracture toughness and flexural strength.

This approach was widely applied to strengthen other important TE materials such as Bi<sub>2</sub>Te<sub>3</sub> based alloys [94] and p-type skutterudites [67], which is beneficial for development of high-strength and high-toughness TE materials and devices.

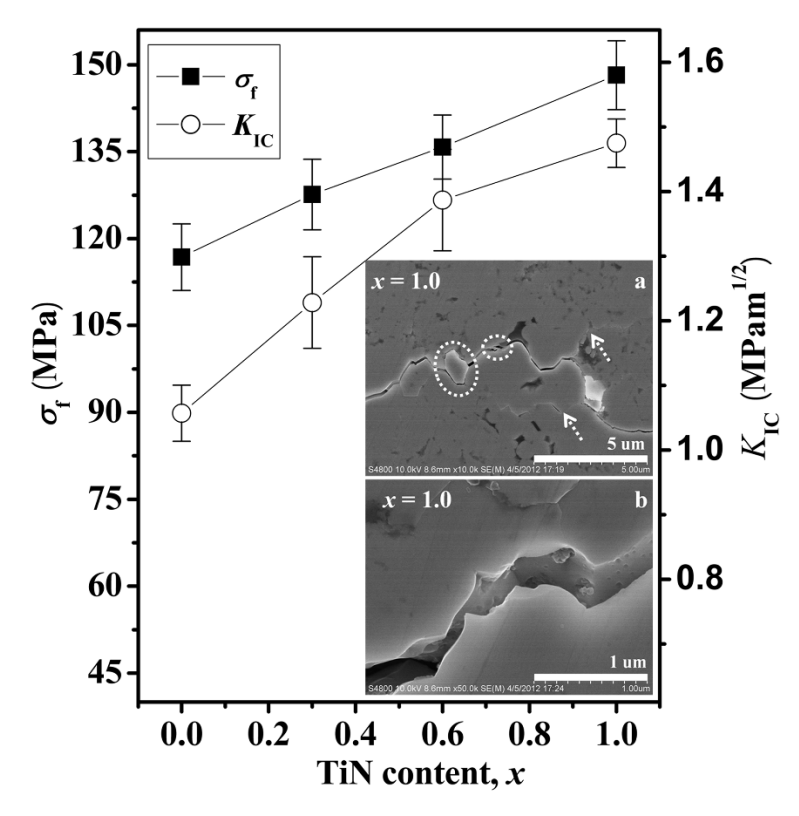


Figure 9 Introducing nano-TiN to strengthen  $CoSb_3$  based TE material [69]. Flexural strength and fracture toughness of  $CoSb_{2.875}Te_{0.125} + x$  vol% TiN composites as a function of TiN content. The embedded figure shows the crack paths in sample containing 1.0 vol% TiN. Reproduction permitted from Elsevier.

#### 5. Conclusions

In this review, we summarized our recent work on fracture toughness of TE materials in three sections:

- (1) The fracture toughness of TE materials can be estimated from intrinsic mechanical properties at the atomic scale. This theoretical method can be extended to ceramics and metals.
- (2) We applied DFT to investigate the tensile and shear deformation properties for several series of important TE materials, providing understanding of the intrinsic mechanical properties at the atomic scale, including ideal strength and fracture mechanisms.
- (3) We found that nanotwin and nanocomposite strategies can improve remarkably the mechanical strength and fracture toughness of TE materials, respectively, which is helpful for development of high performance TE devices with high conversion efficiency and excellent mechanical reliability.

## Acknowledgements

This work is partially supported by the NSFC (No. 51972253), Fundamental Research Funds for the Central Universities (WUT: 2019IVA055, 2019IB006, 2019III208). S.M. is thankful for the support by Act 211 Government of the Russian Federation, under No. 02.A03.21.0011 and by the Supercomputer Simulation Laboratory of South Ural State University. U.A. gratefully acknowledge the financial support provided by the Scientific and Technological Research Council

of Turkey (TÜBİTAK) with grant number 118M371. W.A.G thanks NSF (CBET-2005250) for support.

### References

- 1. Zhu, T.J., et al., *Compromise and Synergy in High-Efficiency Thermoelectric Materials*. Advanced Materials, 2017. **29**(14).
- 2. He, J. and T.M. Tritt, *Advances in thermoelectric materials research: Looking back and moving forward.* Science, 2017. **357**(6358).
- 3. Toberer, E., Solar thermoelectric generators: Pushing the efficiency up. Nature Energy, 2016. **1**(11): p. 16172.
- 4. Liu, W.D., et al., *Ag doping induced abnormal lattice thermal conductivity in Cu2Se+.* Journal of Materials Chemistry C, 2018. **6**(48): p. 13225-13231.
- 5. Li, J., et al., *High-Performance GeTe Thermoelectrics in Both Rhombohedral and Cubic Phases.* Journal of the American Chemical Society, 2018. **140**(47): p. 16190-16197.
- 6. Pennelli, G., *Review of nanostructured devices for thermoelectric applications.* Beilstein J Nanotechnol, 2014. **5**: p. 1268-84.
- 7. Liu, K.G., et al., *Synthesis and characterization of Cu2Se prepared by hydrothermal co-reduction.* Journal of Alloys and Compounds, 2009. **484**(1-2): p. 674-676.
- 8. Li, L., et al., Radical aryl migration enables diversity-oriented synthesis of structurally diverse medium/macroor bridged-rings. Nature Communications, 2016. **7**.
- 9. Wu, X.X., et al., *CUG-binding protein 1 regulates HSC activation and liver fibrogenesis*. Nature Communications, 2016. **7**.
- 10. Qiu, Z.Y., et al., *Spin-current probe for phase transition in an insulator*. Nature Communications, 2016. **7**.
- 11. Zhao, Y.H., et al., *Dectin-1-activated dendritic cells trigger potent antitumour immunity through the induction of Th9 cells.* Nature Communications, 2016. **7**.
- 12. Wang, M., et al., Wars2 is a determinant of angiogenesis. Nature Communications, 2016. 7.
- 13. Fan, Q., et al., *Meta-analysis of gene-environment-wide association scans accounting for education level identifies additional loci for refractive error.* Nature Communications, 2016. **7**.
- 14. Zhou, Q.J., et al., *The primed SNARE-complexin-synaptotagmin complex for neuronal exocytosis.* Nature, 2017. **548**(7668): p. 420-+.
- 15. Heremans, J.P., et al., *Enhancement of thermoelectric efficiency in PbTe by distortion of the electronic density of states.* Science, 2008. **321**(5888): p. 554-557.
- 16. Hua, T., et al., *Crystal structures of agonist-bound human cannabinoid receptor CB1.* Nature, 2017. **547**(7664): p. 468-+.
- 17. Pei, Y.Z., et al., *Convergence of electronic bands for high performance bulk thermoelectrics*. Nature, 2011. **473**(7345): p. 66-69.

- 18. Shi, X., et al., Multiple-filled skutterudites: high thermoelectric figure of merit through separately optimizing electrical and thermal transports. J Am Chem Soc, 2011. **133**(20): p. 7837-46.
- 19. Zheng, Z., et al., Rhombohedral to Cubic Conversion of GeTe via MnTe Alloying Leads to Ultralow Thermal Conductivity, Electronic Band Convergence, and High Thermoelectric Performance. Journal of the American Chemical Society, 2018. **140**(7): p. 2673-2686.
- 20. Zhang, Q., et al., Realizing a thermoelectric conversion efficiency of 12% in bismuth telluride/skutterudite segmented modules through full-parameter optimization and energy-loss minimized integration. Energy Environ. Sci., 2017. **10**(4): p. 956-963.
- 21. Xu, B.A., et al., *Highly Porous Thermoelectric Nanocomposites with Low Thermal Conductivity and High Figure of Merit from Large-Scale Solution-Synthesized Bi2Te2.5Se0.5 Hollow Nanostructures.* Angewandte Chemie-International Edition, 2017. **56**(13): p. 3546-3551.
- 22. Xin, J., et al., Mg vacancy and dislocation strains as strong phonon scatterers in Mg 2 Si 1–x Sb x thermoelectric materials. Nano Energy, 2017. **34**: p. 428-436.
- 23. Su, X., et al., Multi-Scale Microstructural Thermoelectric Materials: Transport Behavior, Non-Equilibrium Preparation, and Applications. Adv Mater, 2017.
- 24. Meng, X., et al., *Grain Boundary Engineering for Achieving High Thermoelectric Performance in n-Type Skutterudites.* Advanced Energy Materials, 2017: p. 1602582.
- 25. Li, W., et al., Promoting SnTe as an Eco-Friendly Solution for p-PbTe Thermoelectric via Band Convergence and Interstitial Defects. Advanced Materials, 2017. **29**(17).
- 26. Zhao, W.Y., et al., *Multi-localization transport behaviour in bulk thermoelectric materials.* Nature Communications, 2015. **6**.
- Tang, Y., et al., *Solubility design leading to high figure of merit in low-cost Ce-CoSb3 skutterudites.* Nat Commun, 2015. **6**: p. 7584.
- 28. Tang, Y., et al., Convergence of multi-valley bands as the electronic origin of high thermoelectric performance in CoSb 3 skutterudites. Nature materials, 2015. **14**(12): p. 1223.
- 29. Kim, S.I., et al., *Thermoelectrics. Dense dislocation arrays embedded in grain boundaries for high-performance bulk thermoelectrics.* Science, 2015. **348**(6230): p. 109-14.
- 30. Liang, T., et al., *Ultra-fast synthesis and thermoelectric properties of Te doped skutterudites.* J. Mater. Chem. A, 2014. **2**(42): p. 17914-17918.
- 31. Li, F., et al., *Polycrystalline BiCuSeO oxide as a potential thermoelectric material.* Energy & Environmental Science, 2012. **5**(5): p. 7188-7195.
- 32. He, J.Q., et al., *Strong Phonon Scattering by Layer Structured PbSnS2 in PbTe Based Thermoelectric Materials*. Advanced Materials, 2012. **24**(32): p. 4440-4444.
- 33. Chang, C., et al., 3D charge and 2D phonon transports leading to high out-of-plane ZT in n-type SnSe crystals. Science, 2018. **360**(6390): p. 778-782.
- 34. Ying, P.J., et al., *Hierarchical Chemical Bonds Contributing to the Intrinsically Low Thermal Conductivity in alpha-MgAgSb Thermoelectric Materials.* Advanced Functional Materials, 2017. **27**(1).
- 35. Chen, Z.W., et al., Lattice Dislocations Enhancing Thermoelectric PbTe in Addition to Band Convergence. Advanced Materials, 2017. **29**(23).

- 36. Zhang, J.W., et al., *Designing high-performance layered thermoelectric materials through orbital engineering.* Nature Communications, 2016. **7**.
- 37. Wei, T.R., et al., Distinct Impact of Alkali-Ion Doping on Electrical Transport Properties of Thermoelectric p-Type Polycrystalline SnSe. J Am Chem Soc, 2016. **138**(28): p. 8875-82.
- 38. Tan, G., L.D. Zhao, and M.G. Kanatzidis, *Rationally Designing High-Performance Bulk Thermoelectric Materials*. Chem Rev, 2016. **116**(19): p. 12123-12149.
- 39. Lin, S.Q., et al., *Tellurium as a high-performance elemental thermoelectric*. Nature Communications, 2016. **7**.
- 40. Hao, S., et al., *Computational Prediction of High Thermoelectric Performance in Hole Doped Layered GeSe.* Chemistry of Materials, 2016. **28**(9): p. 3218-3226.
- 41. Duan, B., et al., *Electronegative guests in CoSb3*. Energy & Environmental Science, 2016. **9**(6): p. 2090-2098.
- 42. Zhu, T., et al., *High Efficiency Half-Heusler Thermoelectric Materials for Energy Harvesting*. Advanced Energy Materials, 2015. **5**(19): p. n/a-n/a.
- 43. Kim, S.I., et al., *Dense dislocation arrays embedded in grain boundaries for high-performance bulk thermoelectrics*. Science, 2015. **348**(6230): p. 109-114.
- 44. Zhao, L.-D., et al., *BiCuSeO oxyselenides: new promising thermoelectric materials*. Energy Environ. Sci., 2014. **7**(9): p. 2900-2924.
- 45. Qiu, Y., et al., *Charge-Compensated Compound Defects in Ga-containing Thermoelectric Skutterudites*. Advanced Functional Materials, 2013. **23**(25): p. 3194-3203.
- 46. Bose, R., et al., *ERF mutations reveal a balance of ETS factors controlling prostate oncogenesis.* Nature, 2017. **546**(7660): p. 671-+.
- 47. Zhao, W.Y., et al., *Superparamagnetic enhancement of thermoelectric performance*. Nature, 2017. **549**(7671): p. 247-+.
- 48. Liu, Z.H., et al., *High thermoelectric performance of alpha-MgAgSb for power generation*. Energy & Environmental Science, 2018. **11**(1): p. 23-44.
- 49. Gao, H., et al., Flux synthesis and thermoelectric properties of eco-friendly Sb doped Mg2Si0.5Sn0.5 solid solutions for energy harvesting. Journal of Materials Chemistry, 2011. **21**(16): p. 5933.
- 50. Liu, W., X. Tang, and J. Sharp, Low-temperature solid state reaction synthesis and thermoelectric properties of high-performance and low-cost Sb-doped Mg2Si0.6Sn0.4. Journal of Physics D: Applied Physics, 2010. **43**(8): p. 085406.
- 51. Nabarro, F.R.N. and F. De Villiers, *Physics of creep and creep-resistant alloys*. 2018: CRC press.
- 52. Frost, H.J. and M.F. Ashby, *Deformation mechanism maps: the plasticity and creep of metals and ceramics*. 1982: Pergamon press.
- 53. El-Desouky, A., et al. *Selective laser melting of a bismuth telluride thermoelectric materials.* in *Proc. Solid Free. Symp.* 2015.
- 54. Hatzikraniotis, E., et al., *Efficiency study of a commercial thermoelectric power generator (TEG) under thermal cycling.* 2010. **39**(9): p. 2112-2116.

- 55. Li, C., G.J. Snyder, and D.C. Dunand, *Compressive creep behaviour of hot-pressed PbTe*. Scripta Materialia, 2017. **134**: p. 71-74.
- 56. Guan, Z.-P. and D.C. Dunand, *Compressive creep behavior of cast Bi2Te3*. Materials Science and Engineering: A, 2013. **565**: p. 321-325.
- 57. Michi, R.A., et al., *Compressive creep behavior of hot-pressed Mg1. 96Alo. 04Sio. 97Bio. 03.* Scripta Materialia, 2018. **148**: p. 10-14.
- 58. Chang, M., et al., *Compressive creep behavior of hot-pressed GeTe based TAGS-85 and effect of creep on thermoelectric properties.* Acta Materialia, 2018. **158**: p. 239-246.
- 59. Al Malki, M., et al., *Creep behavior and postcreep thermoelectric performance of the n-type half-Heusler alloy Hf0. 3Zr0. 7NiSn0. 98Sb0. 02.* Journal of Materials Today Physics, 2019. **9**: p. 100134.
- 60. Muath M. Al Malki, X.S., Pengfei Qiu, G. Jeffrey Snyder, David C. Dunand, *Creep behavior and post-creep thermoelectric performance of the n-type Skutterudite alloy Yb0.3Co4Sb12*. Journal of Materiomics, 2020.
- 61. El-Genk, M.S., et al., *Tests results and performance comparisons of coated and un-coated skutterudite based segmented unicouples.* Energy Conversion and Management, 2006. **47**(2): p. 174-200.
- 62. Zhao, D.G., H.R. Geng, and L.D. Chen, *Microstructure Contact Studies for Skutterudite Thermoelectric Devices.* International Journal of Applied Ceramic Technology, 2012. **9**(4): p. 733-741.
- 63. Bae, K.H., et al., *Power-Generation Characteristics After Vibration and Thermal Stresses of Thermoelectric Unicouples with CoSb3/Ti/Mo(Cu) Interfaces.* Journal of Electronic Materials, 2015. **44**(6): p. 2124-2131.
- 64. Qiu, J., et al., 3D Printing of highly textured bulk thermoelectric materials: mechanically robust BiSbTe alloys with superior performance. Energy & Environmental Science, 2019. **12**(10): p. 3106-3117.
- 65. Liu, Z., et al., Mechanical properties of nanostructured thermoelectric materials  $\alpha$ -MgAgSb. Scripta Materialia, 2017. **127**: p. 72-75.
- 66. Ruan, Z.W., et al., *Low-Cycle Fatigue Properties of CoSb3-Based Skutterudite Compounds*. Journal of Electronic Materials, 2010. **39**(9): p. 2029-2033.
- 67. Peng, S.Y., et al., *Enhanced thermoelectric and mechanical properties of p-type skutterudites with in situ formed Fe3Si nanoprecipitate*. Inorganic Chemistry Frontiers, 2017. **4**(10): p. 1697-1703.
- 68. Zhao, L.D., et al., *Thermoelectric and mechanical properties of nano-SiC-dispersed Bi2Te3 fabricated by mechanical alloying and spark plasma sintering*. Journal of Alloys and Compounds, 2008. **455**(1-2): p. 259-264.
- 69. Duan, B., et al., Enhanced thermoelectric and mechanical properties of Te-substituted skutterudite via nano-TiN dispersion. Scripta Materialia, 2012. **67**(4): p. 372-375.
- 70. Shi, X., et al., *Room-temperature ductile inorganic semiconductor.* Nature Materials, 2018. **17**(5): p. 421-+.
- 71. Li, G., et al., *Enhanced Strength Through Nanotwinning in the Thermoelectric Semiconductor InSb.* Physical Review Letters, 2017. **119**(21): p. 215503.
- 72. Li, G., et al., Superstrengthening Bi\_{2}Te\_{3} through Nanotwinning. Phys Rev Lett, 2017. **119**(8): p. 085501.

- 73. Irwan, *Analysis of Stresses and Strains near the End of a Crack Travelling a Plane.* J. Appl. Mech, 1957. **24**: p. 361-364.
- 74. Hess, B., B.J. Thijsse, and E. Van der Giessen, *Molecular dynamics study of dislocation nucleation from a crack tip.* Physical Review B, 2005. **71**(5).
- 75. Cheng, Y., M.X. Shi, and Y.W. Zhang, Atomistic simulation study on key factors dominating dislocation nucleation from a crack tip in two FCC materials: Cu and Al. International Journal of Solids and Structures, 2012. **49**(23-24): p. 3345-3354.
- 76. Orowan, E., *Brittleness and the Strength of Metals*. Transactions, Institution of Engineers and Shipbuilders in Scotland, 1945. **89**: p. 165-215.
- 77. Li, G., et al., Enhanced ideal strength of thermoelectric half-Heusler TiNiSn by sub-structure engineering. J. Mater. Chem. A, 2016. **4**(38): p. 14625-14636.
- 78. Li, G., et al., *Brittle Failure Mechanism in Thermoelectric Skutterudite CoSb3*. Chemistry of Materials, 2015. **27**(18): p. 6329-6336.
- 79. Li, G., et al., *Micro-and Macromechanical Properties of Thermoelectric Lead Chalcogenides*. ACS applied materials & interfaces, 2017. **9**(46): p. 40488-40496.
- 80. Li, G., et al., *Intrinsic mechanical behavior of MgAgSb thermoelectric material: An ab initio study.* Journal of Materiomics, 2020. **6**(1): p. 24-32.
- 81. Li, G.D., et al., *Determining ideal strength and failure mechanism of thermoelectric CuInTe2 through quantum mechanics.* Journal of Materials Chemistry A, 2018. **6**(25): p. 11743-11750.
- 82. Li, G., et al., Mechanical properties of thermoelectric lanthanum telluride from quantum mechanics. Journal of Physics D: Applied Physics, 2017. **50**(27): p. 274002.
- 83. Li, G., et al., *Deformation mechanisms in high-efficiency thermoelectric layered Zintl compounds*. J. Mater. Chem. A, 2017. **5**(19): p. 9050-9059.
- 84. Li, G., et al., Mechanical properties in thermoelectric oxides: Ideal strength, deformation mechanism, and fracture toughness. Acta Materialia, 2018.
- 85. Li, G.D., et al., *Ductile deformation mechanism in semiconductor alpha-Ag2S*. Npj Computational Materials, 2018. **4**.
- 86. Li, G., et al., *Ideal Strength and Deformation Mechanism in High-Efficiency Thermoelectric SnSe.* Chemistry of Materials, 2017. **29**(5): p. 2382-2389.
- 87. Ogata, S., J. Li, and S. Yip, *Ideal pure shear strength of aluminum and copper.* Science, 2002. **298**(5594): p. 807-811.
- 88. Casper, F., et al., *Half-Heusler compounds: novel materials for energy and spintronic applications.* Semiconductor Science and Technology, 2012. **27**(6).
- 89. van de Walle, A., M. Asta, and G. Ceder, *The Alloy Theoretic Automated Toolkit: A user guide.* Calphad-Computer Coupling of Phase Diagrams and Thermochemistry, 2002. **26**(4): p. 539-553.
- 90. Alexandrov, I.V. and R.G. Chembarisova, *Development and application of the dislocation model* for analysis of the microstructure evolution and deformation behavior of metals subjected to severe plastic deformation. Reviews on Advanced Materials Science, 2007. **16**(1-2): p. 51-72.
- 91. Ogata, S., et al., *Ideal shear strain of metals and ceramics*. Physical Review B, 2004. **70**(10).

- 92. Zheng, Y., et al., *Mechanically Robust BiSbTe Alloys with Superior Thermoelectric Performance: A Case Study of Stable Hierarchical Nanostructured Thermoelectric Materials.* Advanced Energy Materials, 2015. **5**(5): p. 1401391.
- 93. Jiang, C. and S.G. Srinivasan, *Unexpected strain-stiffening in crystalline solids.* Nature, 2013. **496**(7445): p. 339-42.
- 94. Zhao, L.D., et al., Enhanced thermoelectric and mechanical properties in textured n-type Bi2Te3 prepared by spark plasma sintering. Solid State Sciences, 2008. **10**(5): p. 651-658.